M3LW-24OR0402027

Light Water Reactor Sustainability Program

Analysis of Deformation and Fracture Mechanisms in the Harvested High-Dose Baffle-Former Bolt with Stress-Corrosion Cracks Formed While in Service

M. Gussev, S. Kang, T. Lach, X. Chen
Oak Ridge National Laboratory

September 2024

U.S. Department of Energy
Office of Nuclear Energy

ORNL/SPR-2024/3605
M3LW-24OR0402027

Analysis of Deformation and Fracture Mechanisms in the Harvested High-Dose Baffle-Former Bolt with Stress-Corrosion Cracks Formed While in Service

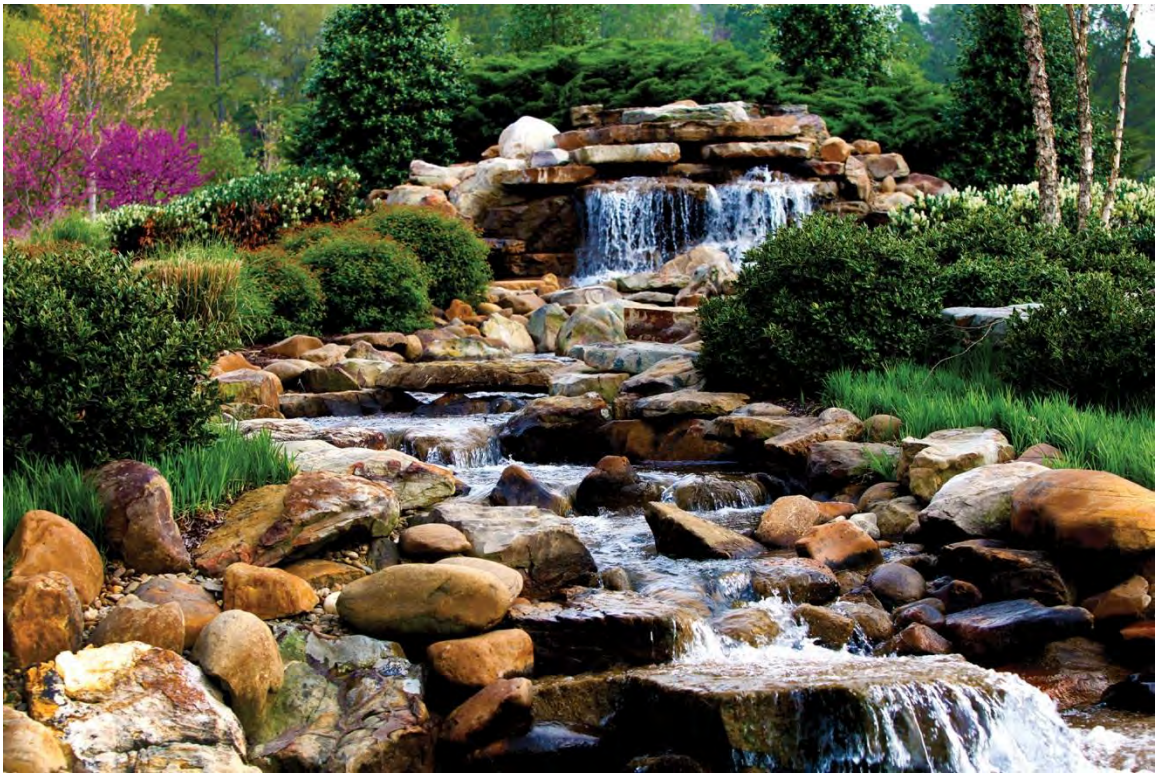

M. Gussev
S. Kang
T. Lach
X. Chen

September 2024

OAK RIDGE National Laboratory

ORNL IS MANAGED BY UT-BATTELLE LLC FOR THE US DEPARTMENT OF ENERGY

ORNL/SPR-2024/3605
M3LW-24OR0402027

Nuclear Energy and Fuel Cycle Division
Materials Science and Technology Division

ANALYSIS OF DEFORMATION AND FRACTURE MECHANISMS IN THE HARVESTED HIGH-DOSE BAFFLE-FORMER BOLT WITH STRESS-CORROSION CRACKS FORMED WHILE IN SERVICE

M. Gussev
S. Kang
T. Lach
X. Chen

September 2024

Prepared under the direction of the
U.S. Department of Energy
Office of Nuclear Energy
Light Water Reactor Sustainability Program
Materials Research Pathway

Prepared by
OAK RIDGE NATIONAL LABORATORY
Oak Ridge, TN 37831
managed by
UT-BATTELLE, LLC
for the
U.S. DEPARTMENT OF ENERGY
under contract DE-AC05-00OR22725

CONTENTS

LIST OF FIGURES

LIST OF TABLES

ABBREVIATIONS

BFB	baffle-former bolt
DOE	US Department of Energy
dpa	displacement per atom
EBSD	electron backscatter diffraction
EDS	energy-dispersive x-ray spectroscopy
GAM	grain average misorientation
GROD	grain reference orientation deviation
IASCC	irradiation-assisted stress corrosion cracking
IPF	inverse pole figure
IQ	image quality
KAM	kernel average misorientation
LAMDA	Low Activation Materials Development and Analysis Laboratory
LWR	light-water reactor
ORNL	Oak Ridge National Laboratory
NPP	nuclear power plant
PWR	pressurized water reactor
ROI	region of interest
SEM	scanning electron microscopy
TE	total elongation
UE	uniform elongation
UTS	ultimate tensile strength
YS	yield strength

ACKNOWLEDGMENTS

This research was supported by the US Department of Energy, Office of Nuclear Energy, Light Water Reactor Sustainability Program, Materials Research Pathway. Valuable help and support from the staff at the Oak Ridge National Laboratory (ORNL) Low Activation Materials Development and Analysis Laboratory (K. Everett, P. Tedder, B. Ensign, S. Curlin) and Radiation Control Technician Office are gratefully acknowledged. The authors thank Dr. P. Doyle (ORNL) for reviewing the report and E. Heinrich (ORNL) for helping with document preparation.

EXECUTIVE SUMMARY

This report presents the results of advanced mechanical testing conducted on miniature tensile specimens excised from an irradiated baffle-former bolt, a commercial pressurized water reactor component. The specimens were extracted from the midsection of the bolt shank, where the estimated damage dose reached 23 displacements per atom.

The mechanical testing included the following tests: (1) conventional tensile testing at room temperature, augmented by digital image correlation (DIC) to enable noncontact strain measurements, and (2) in situ tensile testing within a scanning electron microscopy (SEM) instrument equipped with energy-dispersive x-ray spectroscopy (EDS) and electron backscatter diffraction (EBSD) detectors to evaluate active deformation and fracture mechanisms.

Additionally, SEM fractographic analysis revealed alterations in the fracture mechanism from a predominantly ductile fracture in nonirradiated steel to a mixed fracture mode (still dominating ductile and minor cleavage spots) in irradiated specimens derived from the baffle bolts.

The findings indicate a complex strain localization behavior for in-service irradiated steel specimens. Beyond conventional necking at the macro scale and defect-free channel formation at the micro scale, DIC results identified the presence of deformation bands approximately 100 μm in width. These bands consist of chains of grains exhibiting elevated local strain levels and may be considered an intermediate or mesoscale level of strain localization.

These bands become discernible near the yield stress as localized hot spots, areas of elevated strain, persisting throughout most of the experiment. The formation of mesoscale deformation bands as a strain localization mechanism may exacerbate the defect-free channel formation in irradiated materials, further promoting irradiation-assisted stress corrosion crack initiation.

1. INTRODUCTION

Baffle-former bolts (BFBs) are critical components in pressurized water reactors (PWRs), ensuring the mechanical integrity of the core assembly that contains fuel elements. During operation, BFBs and other in-core components are subjected to complex radiation-induced degradation exacerbated by the corrosive environment. The degradation of BFBs, particularly irradiation-assisted stress corrosion cracking (IASCC), has been a significant concern for the nuclear industry since the 1980s.

To investigate the long-term operational performance and reliability of in-core components and to support the extension of PWR lifetimes, the US Department of Energy (DOE) Light Water Reactor Sustainability Program's Materials Research Pathway undertook an effort to harvest two high-fluence BFBs from a commercial Westinghouse two-loop downflow-type PWR. In 2016, these high-fluence BFBs were successfully harvested from a Westinghouse PWR and delivered to the Westinghouse hot-cell facility for specimen fabrication. The fabricated specimens were then sent to Oak Ridge National Laboratory (ORNL) for fracture mechanics testing [1,2], microstructural analysis [3,4], and advanced mechanical testing [5].

Microstructural analysis revealed several notable phenomena: the observation of in-service-formed dislocation channels was among the most significant [6]. These dislocation channels were identified in samples taken from the head-to-shank transition area of the BFB. The channels exhibited secondary radiation-induced segregation and the formation of a new generation of radiation defects after channel formation [6]. Researchers concluded that at least one loading event occurred during service with stress levels approaching the yield stress. Several short intergranular cracks accompanied these defect-free channels.

This report builds on previous studies of active deformation mechanisms and strain localization in BFBs [3,5]. The latest results provide further insights into localized strain behavior in heavily irradiated austenitic steels.

2. MATERIALS

2.1 HARVESTED BAFFLE-FORMER BOLTS

Table 1 provides information on bolt IDs, range of fluences, and estimated displacement damage doses [1,4]. Additional information (irradiation temperature profile, flux) is not available.

Table 1. Fluence and estimated displacement damage distributions for two retrieved BFBs

Bolt ID	Fluence (10^{22} n/cm^2, E > 1 MeV) and estimated damage dose for different portions of BFBs (dpa)					
	Head (CS) specimens		Mid-shank (MS) specimens		Mid-thread (BS) specimens	
	Fluence	Dose*	Fluence	Dose*	Fluence	Dose*
4412	2.78	41	2.27	34	1.46	22
4416	1.91	29	1.56	23	1.00	15

* Fluence values were converted to displacement damage, assuming a fluence-to-displacements per atom (dpa) conversion value of 6.7×10^{20} n/cm^2, E > 1 MeV/dpa [7].

The specimen machining scheme and specimen IDs are shown in Figure 1. For each BFB, four bend-bar specimens and seven thin-slice specimens were machined. The bend-bar specimens were used in the fracture toughness and fatigue crack growth rate studies [2]. The thin-slice specimens were designated for microstructural analyses [3] and advanced mechanical testing [5].

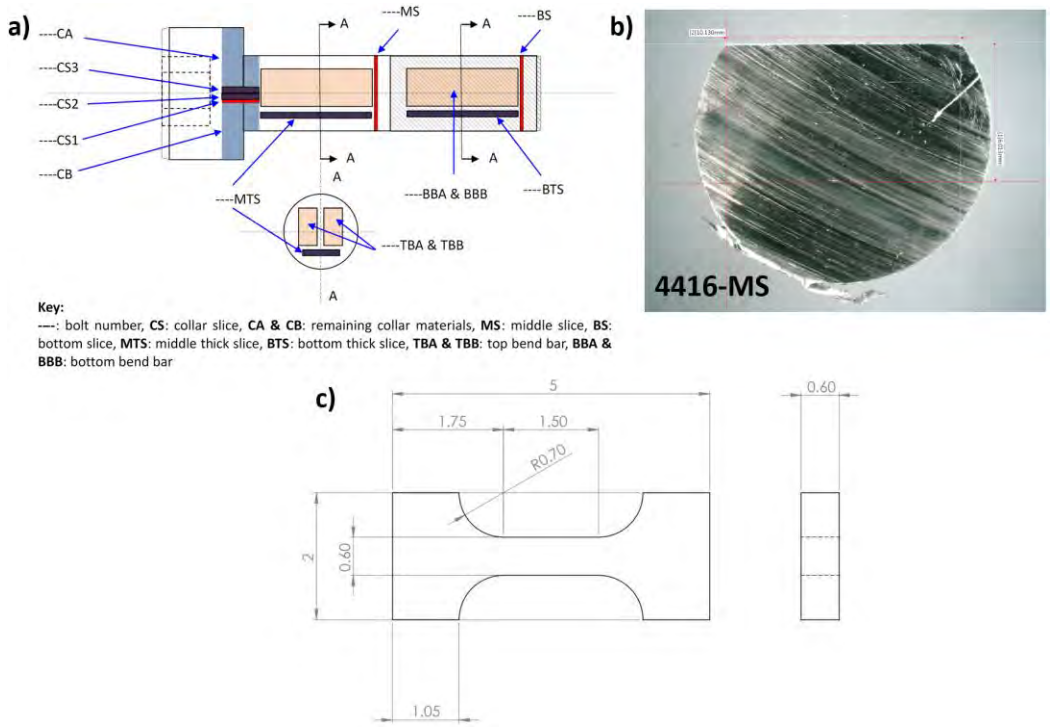

Figure 1. Specimen machining scheme and specimen IDs. (a) Bolt cutting scheme and IDs for cut objects [1], (b) image of the MS-slice used in the present work; miniature tensile specimen geometry and dimensions (in millimeters). References [1,2,4] provide more detail.

Miniature tensile specimens were machined from the mid-shank slice (MS; Figure 1. shows specimen location) using electric discharge machining (EDM). The specimens had gauge dimensions of 1.5 mm (length) by 0.6 mm (width) by 0.6 mm (thickness). Specimen IDs and specimen usage are summarized in Table 2.

Conventional tensile test accompanied by DIC strain measurements (Section 2.2) was performed with Specimen 4416-MS-2, yielding interesting results (Section 3.3). Because previous work showed a tendency for cracks to form along the gauge, a tensile test at a slower strain rate (10^{-5} s^{-1}) was attempted using Specimen 4416-MS-4; unfortunately, equipment failure occurred, compromising the results. In the future, adding a modern specialized tensile frame with the capability for slow strain rate testing (ranging from 10^{-5} to 10^{-7} s^{-1} for specimen gauge lengths of approximately 1.5 to 25 mm) would significantly enhance LAMDA's capabilities.

Specimen 4416-MS-2 was designated for in situ SEM/EBSD experiments (Sections 2.3 and 3.4).

Table 2. Experiment list with MS-tensile specimens

Specimen ID	Specimen use	
4416-MS-2	In situ SEM/EBSD test	Successful.
4416-MS-3	Tensile DIC test at $10^{-3}s^{-1}$	Successful.
4416-MS-4	Tensile DIC test at $10^{-5}s^{-1}$	Equipment failure.

Microstructure analysis was performed using a TESCAN MIRA3 SEM instrument equipped with an Oxford Symmetry EBSD detector and an Oxford Ultim Max 170 EDS detector.

2.2 DIC-ASSISTED TENSILE TEST

Tensile tests were conducted using an MTS 10 kN two-column tensile screw machine located in the hot area of LAMDA. The specimens were shoulder-loaded using specialized grips and tested at room temperature under a nominal strain rate of 10^{-3} s^{-1} (corresponding to a displacement rate of 0.09 mm/min for the employed specimen geometry). Noncontact strain measurements were carried out via the digital image correlation (DIC) technique [8–10], the principles, advantages, and limitations of which are discussed in detail elsewhere.

Immediately before testing, the specimen surface was coated with white and black paint to generate a random speckle pattern. An Allied Vision GX3300 digital camera, paired with a telecentric lens, was used to capture images of the specimen during testing at a frequency of 1 Hz (i.e., one image per second). The optical resolution achieved was approximately 2.64 μm per pixel. After testing, 2D strain fields and strain rate values were computed using VIC-2D commercial software in conjunction with a custom DIC code. The custom DIC code employs Newton–Raphson-type algorithm [11,12] and includes all recently offered modifications, including inverse calculation of the Hessian matrix [13] and bicubic splines for source image interpolation. In contrast to commercial DIC codes, no smoothing is performed over the calculated strain fields to maintain spatial resolution. Raw data fields allow the analyst to decide on the origin and nature of the calculated values.

2.3 IN SITU SEM/EBSD ASSISTED EXPERIMENT

To perform an in situ SEM/EBSD experiment, the tensile specimen was mechanically ground and polished using a Minimet device and, after that, electropolished using Struers A2 solution at 30 V DC for 5–7 s. Mechanical grinding and electropolishing fully remove EDM-induced remelted layers from the flat portions of the specimen.

The mechanical test was performed at room temperature at a strain rate of 10^{-3} s^{-1} using the Kammrath & Weiss 5 kN tensile stage [4]. The experiment was conducted inside TESCAN MIRA3 SEM instrument, which is equipped with an Oxford Symmetry EBSD detector and an Oxford Ultim Max 170 EDS detector [14]. The experiment workflow (selection of region of interest, deformation steps, local strain assessment) was identical to in situ testing approach described elsewhere [14,15].

3. EXPERIMENTAL RESULTS

3.1 BFB BASIC MICROSTRUCTURE

Figure 2 shows a representative MS-slice microstructure recorded for one of the machined miniature tensile specimens before the start of a tensile test. An equiaxial grain microstructure with well-shaped grains containing multiple annealing twins is visible. No ferrite was reliably observed in the microstructure, so no phase map is shown. The image quality (IQ) map suggests the presence of some nonmetallic inclusions of a few micrometers in size; the inclusions' density is limited and not of major concern.

The EBSD data suggest mostly annealed microstructure, with minor misorientation gradients; however, some grains contain slightly elevated misorientation levels (as shown in the grain reference orientation deviation [GROD] map). The presence of in-grain orientation gradients indicates deformation before irradiation, likely during component manufacturing. An interesting case is the grain marked as "GC" ("grain with channels") with obvious dislocation channel microstructure. These features are distinctly different from smooth misorientation gradients that usually form during deformation in nonirradiated steel. The appearance of grains with channels ("GC" in Figure 2) suggests a deformation event after irradiation, probably during BFB extraction.

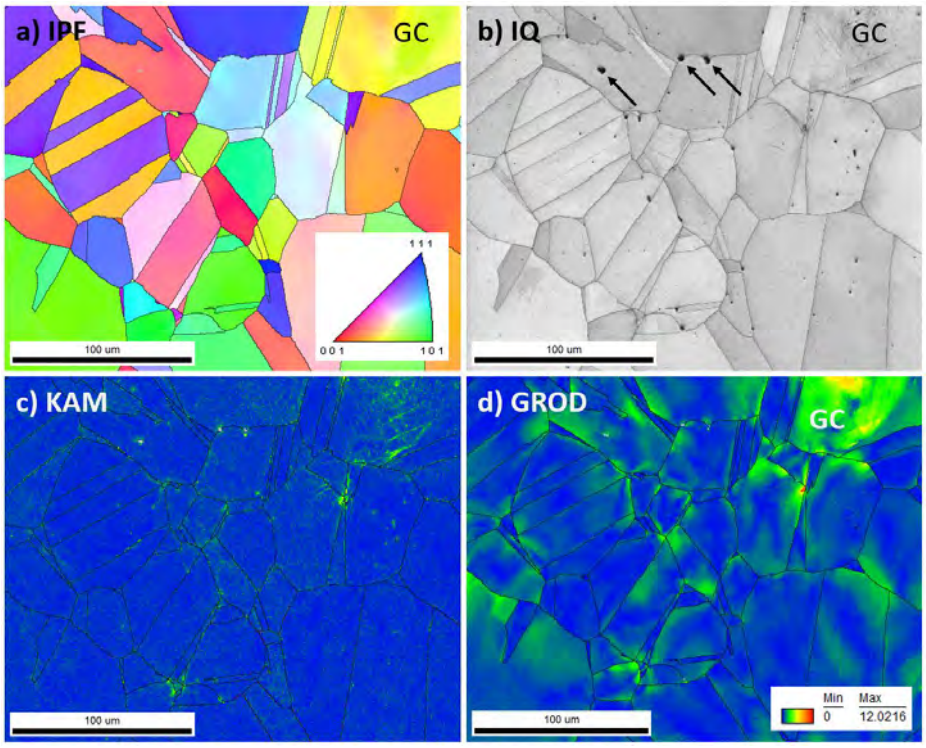

Figure 2. Microstructure of the 4416-MS-2 tensile specimen (SEM/EBSD maps recorded approximately at the middle of the gauge. Figure 1 shows the MS slice and specimen location). An equiaxial grain microstructure is visible. Black arrows in IQ map point to nonmetallic inclusions. A grain with defect-free channels is marked as GC. No second phase (body-centered cubic ferrite) appeared in the scans, so the phase map is not shown. The inverse pole figure (IPF) color key is the same for all images in the document. All IPFs in the present report are colored in the horizontal (tensile) direction.

3.2 TENSILE PROPERTIES OF THE BFB SPECIMENS

Figure 3 presents the engineering tensile curve for the 4416-MS-3 tensile specimen deformed at room temperature. The specimen exhibited significant radiation hardening, with yield strength (YS) and ultimate tensile strength (UTS) measured at approximately 1,006 MPa and 1,046 MPa, respectively (Table 3). The nominal uniform elongation (UE) was 1.52%, indicating pronounced radiation embrittlement. The total elongation (TE) reached 26.42%, which is relatively high for the corresponding damage dose level. The TE value is sensitive to specimen geometry. Although the miniature specimen geometry used for this test reliably reproduces YS, UTS, and UE, it tends to overestimate the TE because of the short gauge length of only 1.5 mm. This scaling effect will be analyzed in more detail in a forthcoming publication.

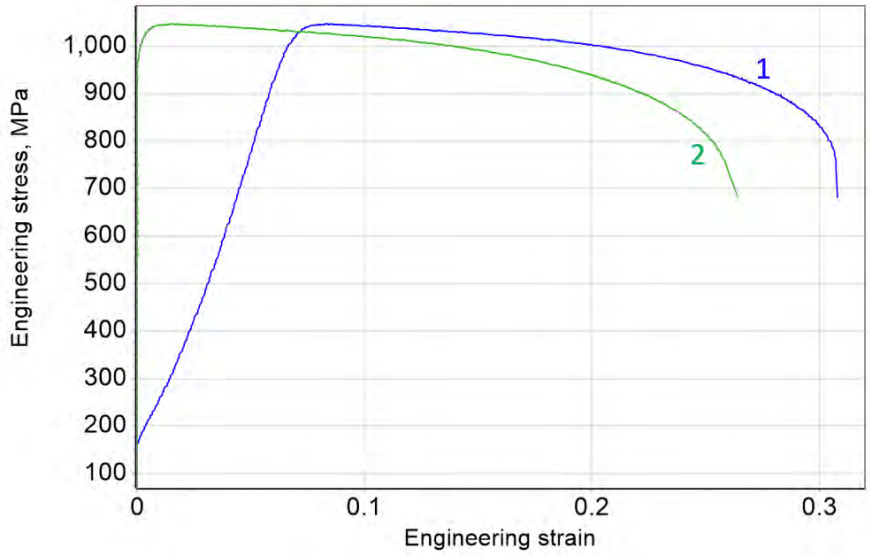

Figure 3. Engineering tensile curve for Specimen 4416-MS-3 deformed with 10^{-3} s^{-1} strain rate. Curve 1: engineering strain–engineering stress (elastic compliance is not removed); Curve 2: plastic strain–engineering stress (elastic compliance and elastic strain are removed).

Table 3. Engineering mechanical properties for the tested specimens

Specimen	Yield stress (MPa)	Ultimate stress (MPa)	Uniform elongation (%)	Total elongation (%)
4416-MS-2	924.5	947.1	1.1	n/a
4416-MS-3	1,006.0	1,046.6	1.5	26.4

Table 3 also provides the mechanical test results for Specimen 4416-MS-2, which was tested in situ inside an SEM instrument (Section 3.4). The YS, UTS, and UE values for this specimen were comparable to those of Specimen 4416-MS-3. The slightly lower strength could be attributed either to normal specimen-to-specimen variation or to differences in cross-sectional geometry; electropolishing can result in rounded edges, leading to a slight overestimation of the cross-sectional area. No TE value is available for this specimen because the test was interrupted before the fracture.

In summary, the YS, UTS, and UE values are consistent with those typically observed in austenitic 300-series steels irradiated in PWRs. Direct comparison of TE with values reported in the literature is challenging because of the short gauge length used in this study. The smooth neck development and

extended descending branch of the tensile curve suggest considerable localized ductility within the neck region.

3.3 DIC ANALYSIS OF STRAIN FIELD EVOLUTION DURING TENSILE TESTING OF BFB SPECIMEN

Figure 4 presents the DIC and statistical analysis results for the 4416-MS-3 tensile specimen cut from baffle bolt #4416. Two artifacts, marked as "A" and enclosed by black dashed ovals, are visible in the DIC data field. These artifacts are attributed to a few damaged pixels in the camera matrix, likely caused by the harsh conditions in the hot area. Because the artifacts remain in fixed spatial positions, they are easily identifiable and can be excluded from the analysis.

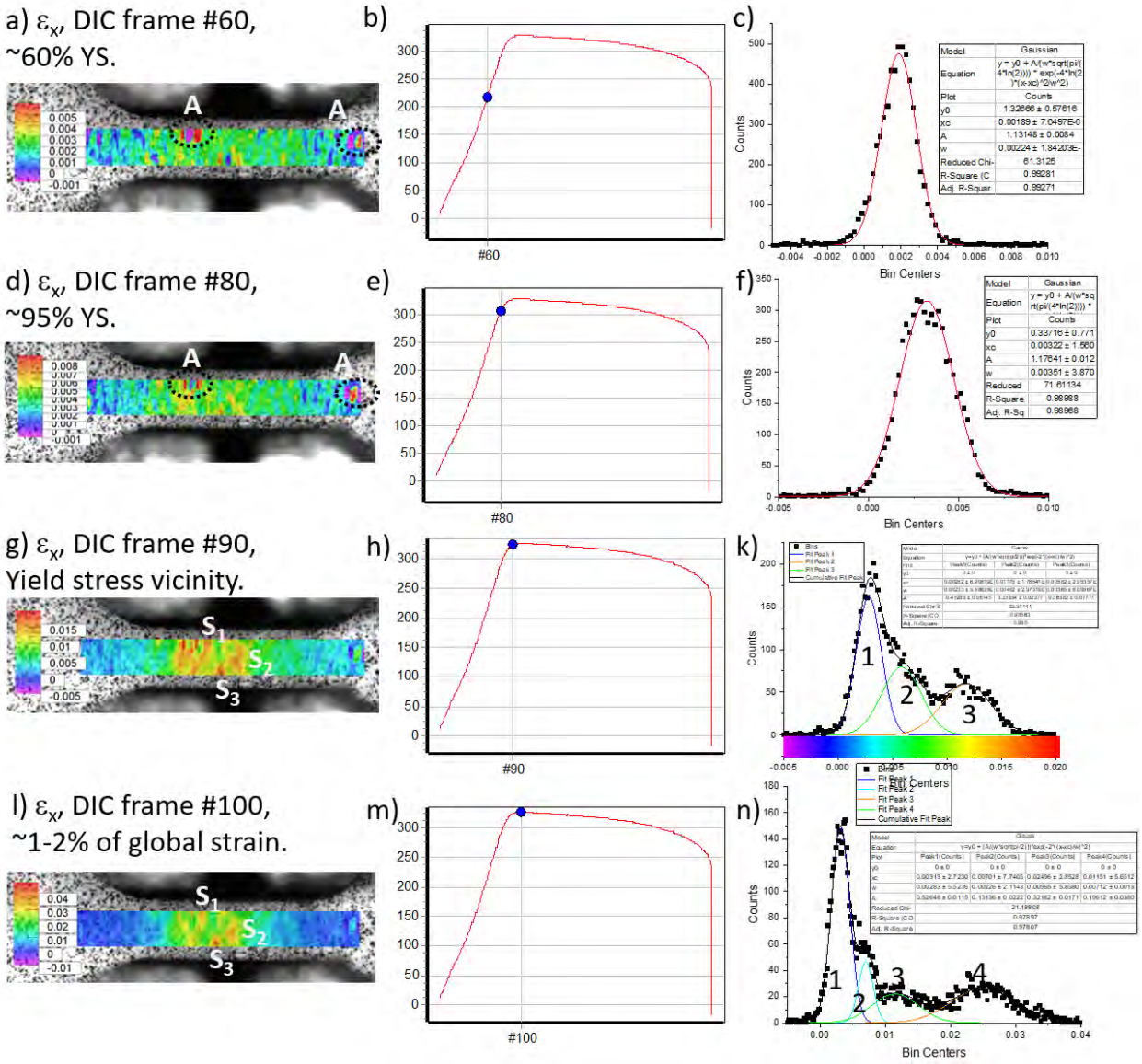

Figure 4. Strain fields in the small strain area (below yield stress and in the small plastic strain area) for 4416-MS-3 miniature specimen tested using the conventional DIC approach. Engineering strain in the tensile direction (*x*-axis) is used. Color scale was added in (k) to help with interpretation of the DIC map shown in (g).

During the experiment, primarily elastic stresses were expected at load levels corresponding to approximately 60%–70% of the yield stress. Although dislocation channels may form below the yield stress level [16], the plastic strain component is considered negligible. Figure 4a displays the 2D strain map at a stress level of approximately 60% YS. The marked point on the tensile curve in Figure 4b indicates the load and displacement values corresponding to the DIC image and associated strain map. Analysis of the strain map reveals that strain values fluctuate around approximately 0.002–0.003 (0.2%–0.3%), which is consistent with elastic strain values for stress levels around 600–700 MPa (~0.30%–0.35%). The map also includes the specimen's heads and shoulders, where lower elastic strains are expected compared with the gauge section.

The strain level in the head region should be slightly above zero, but, owing to inevitable noise from DIC data processing algorithms, values fluctuate between approximately −0.001 and +0.002. The average strain level in the gauge section is about 0.003, although some localized values are likely influenced by random noise.

When represented as a histogram, shown in Figure 4c, the strain dataset exhibits a bell-shaped (Gaussian) distribution. A single Gaussian curve provides a good approximation of the DIC data at this load level. Although two distinct curves—corresponding to the elastic strains in the specimen heads and the gauge section—might be expected, the difference between these regions is too small, comparable to the DIC uncertainty, so the curves are impossible to separate at this stress level. The width of the bell curve, approximately 0.002 in strain terms, suggests a DIC inaccuracy of about 2,000 με.

As the specimen approached approximately 95% of the YS (Figure 4d, e), the DIC map shows a slight increase in strain values. The corresponding strain histogram (Figure 4f) remains largely unchanged, although the peak broadens. This peak widening (w-value increasing from ~0.002 to ~0.0035) reflects a growing strain difference between the heads and the gauge, as well as the transition from primarily elastic to elastic–plastic deformation in the gauge region.

Near the YS (Figure 4g, h), at a strain level corresponding to 0.2% plastic strain, the strain map reveals several localized strain maxima along the gauge. These maxima, with amplitudes reaching up to about 0.015 (1.5%), indicate plastic strains and a mixed elastic–plastic deformation mode at these points. Notably, the distribution of strain maxima (~0.012–0.015, shown in orange and red on the DIC map) and minima (~0.006–0.01, shown in green) along the gauge is of particular interest. The difference between them (~0.004–0.005) exceeds the estimated DIC inaccuracy and suggests an underlying physical process responsible for the observed strain fluctuations.

The strain data histogram in Figure 4k displays three distinct peaks. The first peak represents the elastic strains in the heads, shoulders, and the undeformed portion of the gauge. The second peak, centered at approximately 0.006, is slightly higher than the expected maximum elastic strain (~0.005 for ~1,000 MPa stress) and corresponds to weak plastic deformation (green areas in the DIC map, Figure 4g). The third peak reflects regions with more significant local strains (orange and red areas in Figure 4g). To facilitate comparison, a color bar has been added to the histogram plot, allowing easy correlation of the peaks with the corresponding regions in the DIC strain map.

For minor plastic strains (~1%), shown in Figure 4l, n, the data reveal four peaks: elastically loaded heads (Peak 1), likely weakly deformed gauge areas and specimen shoulders (Peak 2), and the deformed portions of the gauge exhibiting smaller and larger deformations (Peaks 3 and 4).

The spatial distribution of many hot spots (areas with elevated local strain) is of particular interest. By comparing Figure 4g, l, the same hot spots (Spots S_1, S_2, and S_3) can be identified, forming specific

spatial patterns. Additionally, Spot S_2 likely appears in Figure 4d as a weakly deformed region, and a similar phenomenon may be observed for Spot S_3.

Figure 5 presents DIC data over a wider strain range, extending from the YS to near the fracture point. At higher strain levels, the integrity of the paint layer, which is essential for accurate DIC calculations, begins to deteriorate and crack, rendering the subsequent DIC data unreliable. Despite this limitation, an analysis of the DIC results reveals that the hot spots identified in Figure 4 can be tracked consistently across the entire strain range.

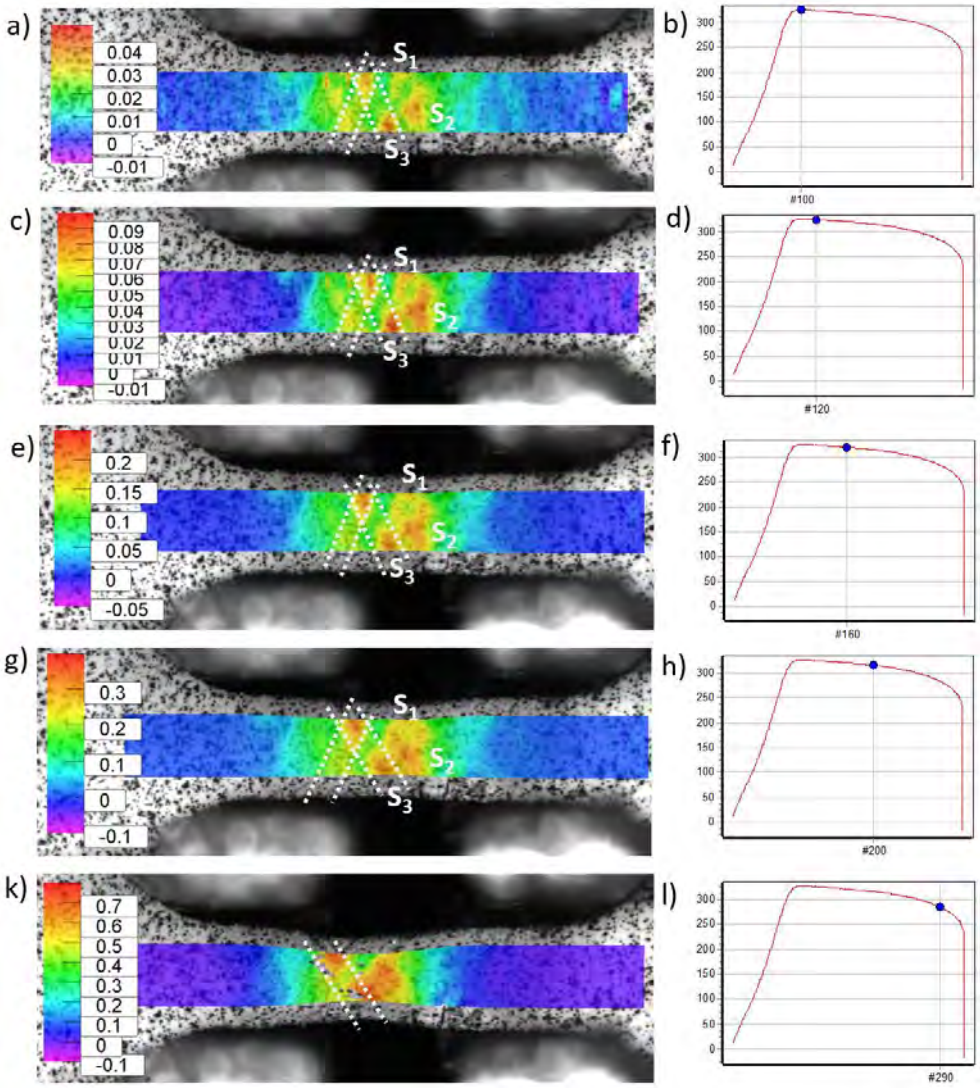

Figure 5. DIC strain maps for moderate and large strain levels; 4416-MS-3 specimen. The maps show engineering strain in the tensile direction (ε_X).

The observed behavior can be preliminarily interpreted as a series of deformation bands, indicated by dashed lines. The interaction between these bands leads to the formation of hot spots at the points where they intersect. These bands' estimated widths range from approximately 100 to 140 μm.

The most notable result of this experiment is the significant strain variation within the growing neck of the small specimen. The difference in strain between the less deformed regions (green) and the more

deformed regions (orange to red) is nearly twofold. The optical resolution of the DIC system (~2.64 μm/pixel) results in a DIC subset of about 32 pixels, which is small enough to encompass only one or two grains. Although conventional DIC cannot detect strain gradients within a subset, variations in the strain field at the grain scale become detectable.

The appearance and evolution of these bands are dynamic processes. Studies on band formation in aluminum alloys [17] and the dynamic strain aging effect in various materials suggest that bands form, develop over time, and then cease evolving. In zirconium alloys, bands can form and persist alongside uniform deformation throughout the entire experiment [18]. However, this phenomenon remains poorly understood in irradiated austenitic steels, and further research is required.

If the strain level and increments within the band are low, then the band may be obscured by previously accumulated strains. To enhance the visualization of bands and hot spots, Figure 6 presents the DIC data using differential strain maps, which show only the strain changes accumulated over a few consecutive images, excluding earlier-developed processes. For instance, Figure 6a depicts the strain changes between image #60 (blue point in Figure 6b) and image #65 (red point). At this stress level, the results mainly reflect elastic strain increments along with some noise.

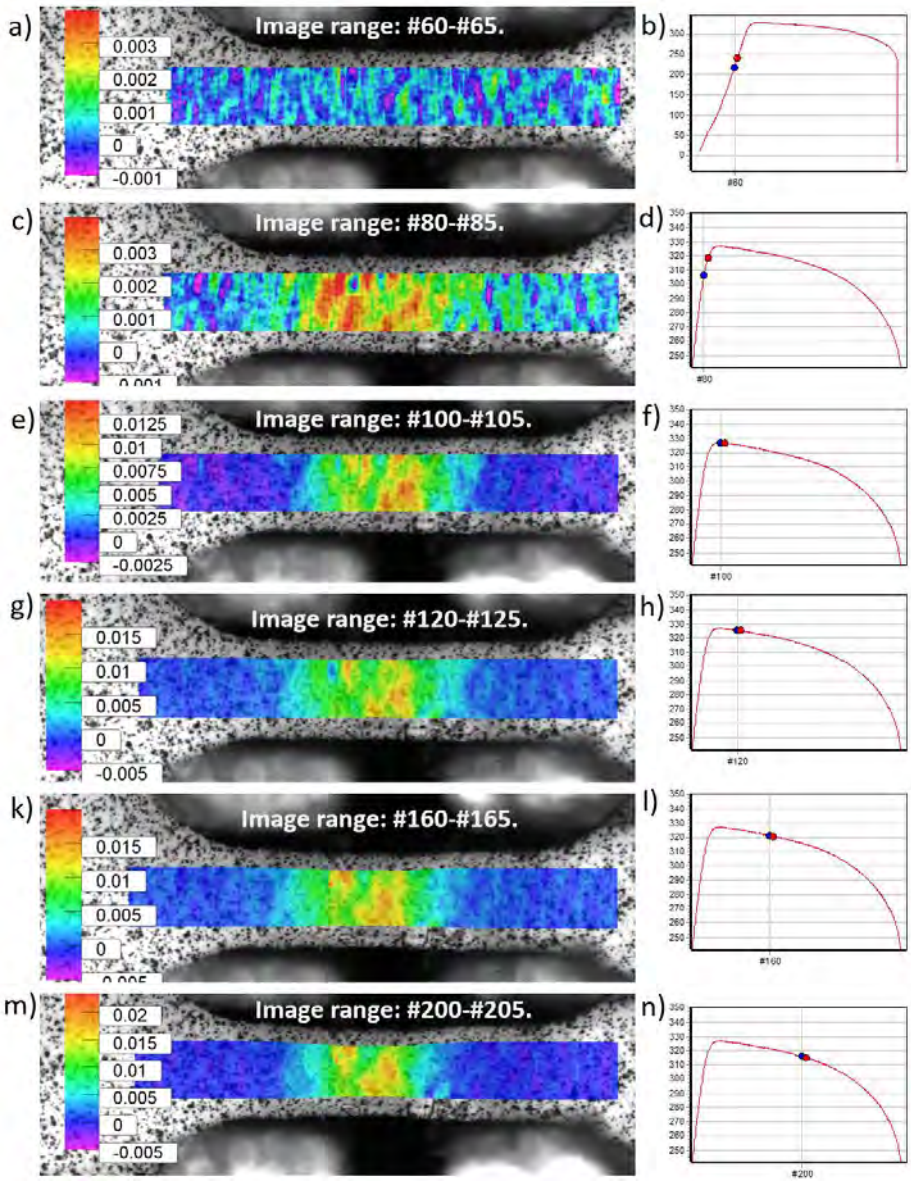

Figure 6. Differential strain rate maps for Specimen 4416-MS-3.

However, as the stress level approaches the YS, shown in Figure 6c, d, localized changes begin to appear in the gauge, with amplitudes up to 0.003—exceeding the expected inaccuracy of approximately 0.002. This result suggests the emergence of localized strain areas.

Further datasets in Figure 6 reveal regions with significantly higher local strain increments compared with the surrounding areas. The hot spots or localized areas with elevated strain maintain their positions throughout the experiment. These differential maps confirm the presence of hot spots that accumulate strain more rapidly. These spots remain active throughout most of the experiment and likely form at or slightly below the yield stress, even though they are initially masked by noise.

In summary, the DIC results indicate that the processes of deformation localization are highly complex and multiscale. Although macroscale necking and microscale dislocation channeling are well-established mechanisms, the DIC analysis reveals an intermediate feature: the formation of deformation bands within the developing neck.

These stationary deformation bands form a distinctive pattern on the specimen surface, emerging as early as the yield stress and persisting with minimal changes throughout the experiment. Intersections of these bands are believed to result in hot spots, (i.e., areas of increased local strain). The width of these bands is estimated to be around 120 µm, corresponding to 1–2 grains or so. The strain profile within a band may follow a bell-like or triangular distribution, with higher strains at the center, suggesting that the bands might be narrower and develop in chains of grains oriented at an angle to the tensile axis. Currently, no generally accepted approach exists for analyzing and deconvoluting such band patterns, allowing only qualitative assessments at this time.

From the IASCC perspective, assuming that the initiation of IASCC is closely linked to localized deformation, the formation of hot spots and the development of deformation bands at small plastic strains—or even below the yield stress—are particularly concerning. These phenomena may accelerate crack initiation, making them potentially detrimental to material performance under irradiation.

3.4 ANALYSIS OF THE SEM/EBSD IN SITU TENSILE TEST RESULTS

The miniature 4416-MS-2 tensile specimen was deformed incrementally, as shown in Figure 7, with the reference step (S00) taken at zero load. EBSD data were recorded at each deformation step, and SEM micrographs were captured for each selected region of interest (ROI) to observe specific developing features.

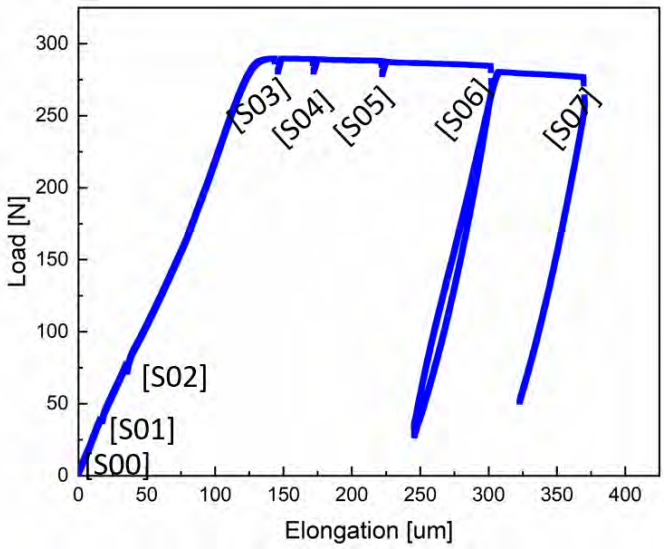

Figure 7. Tensile curve recorded during in situ experiment and showing the experiment interruptions to perform EBSD scans. Specimen ID: 4416-MS-2.

Steps S01 and S02 were conducted within the elastic load range, below the macroscopic yield stress. These datasets are intended to provide additional statistical insights and assess the feasibility of calculating total strains (both elastic and plastic) from EBSD data, as well as to account for SEM image distortion. However, these aspects are beyond the scope of this report. Step S03 was performed at a small plastic strain of approximately 2%.

In this heavily irradiated austenitic steel, necking began immediately after reaching the yield stress, limiting the extent of uniform deformation. A total of five deformation steps (S03–S07) were conducted in the plastic deformation region.

Figure 8 shows the overall view of the specimen at different deformation steps. Once the YS is reached and exceeded, the specimen enters the elastic–plastic deformation phase. Visible surface roughness begins to develop on the right side of the gauge, indicating plastic deformation processes and the formation and evolution of dislocation channels. The "active" plastically deforming region gradually expands to cover roughly half of the total gauge length as the experiment progresses.

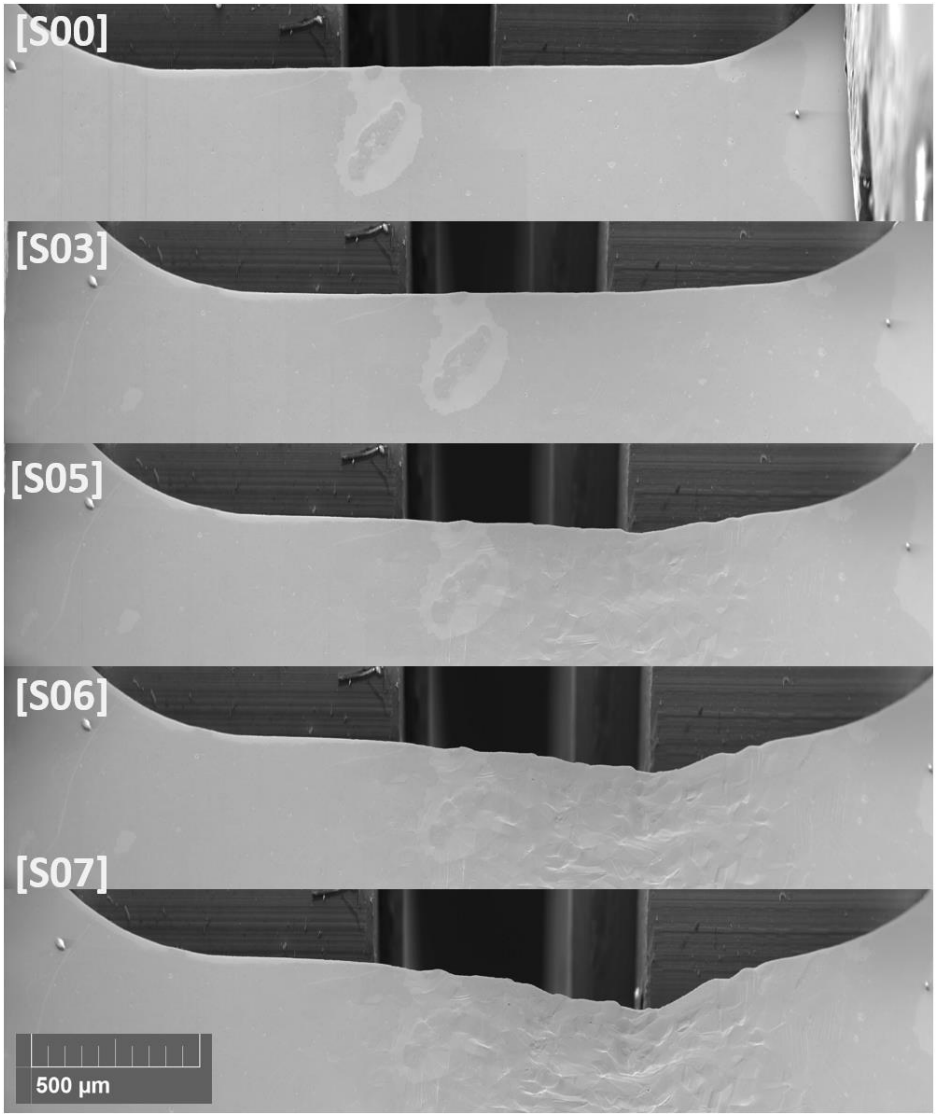

Figure 8. A collage showing low-magnification images recorded at different strain steps. A visible neck develops at the right side of Specimen 4416-MS-2.

Although minor microfracture events were observed, they were primarily associated with small nonmetallic inclusions. No significant cracking occurred in this specimen. After a pronounced neck formed at Step 7 (S07), the experiment was halted at approximately 350 µm total elongation to avoid the risk of specimen fracture within the SEM chamber.

3.4.1 Microstructure Evolution and Active Deformation Mechanisms

Figure 9 presents a typical EBSD dataset for a selected ROI. A typical ROI includes approximately 20–30 grains with varying orientations, providing sufficient statistical data. The inverse pole figure (IPF) maps

within the EBSD dataset illustrate grain morphology and orientation; the color-coded representation of lattice orientations is particularly useful for identifying strain-induced changes. The IQ map indicates the quality of the Kikuchi patterns: lower (darker) IQ values signify poorer pattern quality and the presence of defects, either on the surface (e.g., slip traces, scratches, etching pits) or within the microstructure (e.g., grain boundaries, dislocation pileups). Kernel average misorientation (KAM) maps show the distribution of dislocations within the structure.

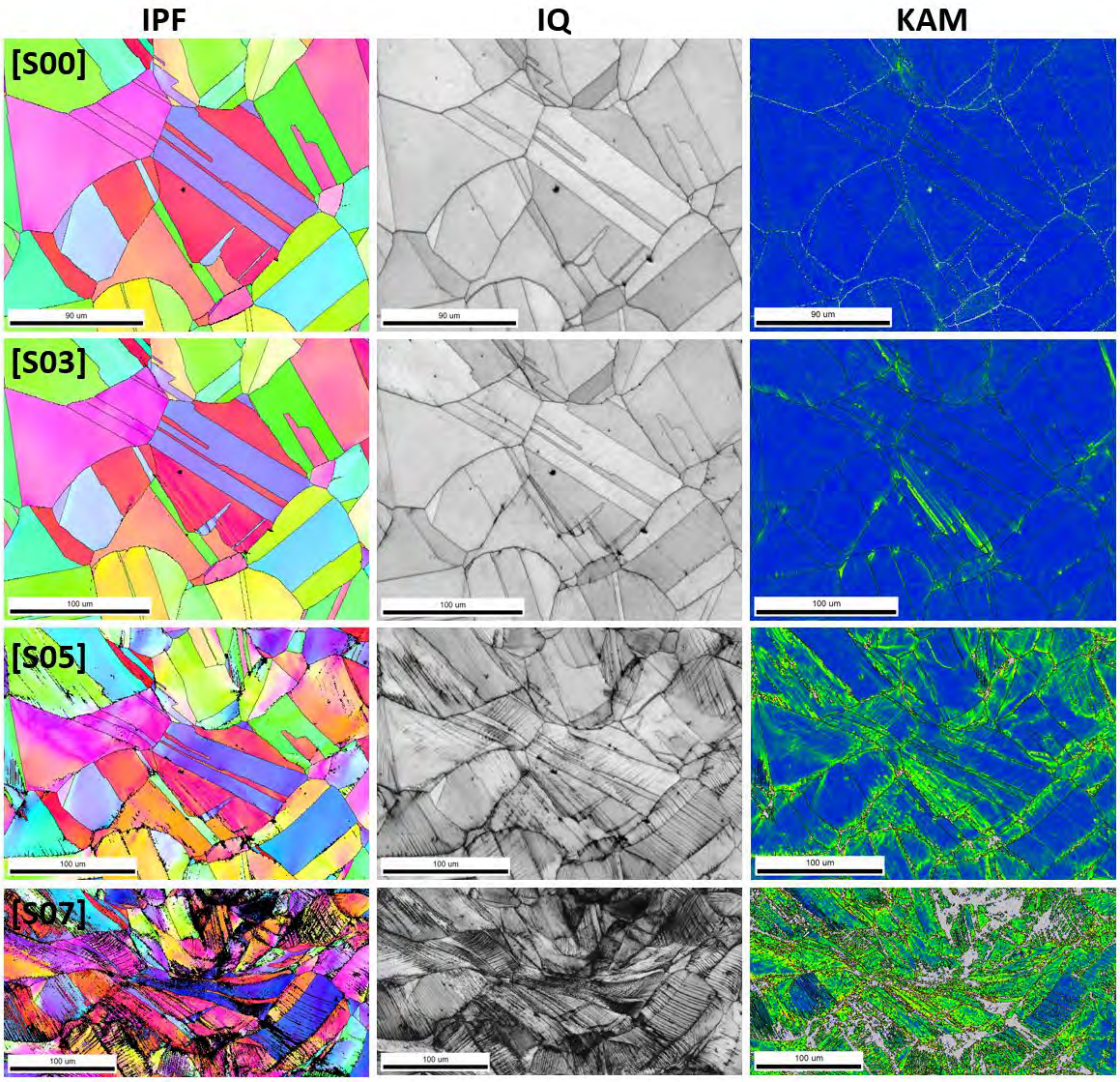

Figure 9. Typical EBSD dataset and its evolution at different strain steps. Specimen ID: 4416-MS-2.

In Figure 9, pronounced changes in lattice orientation are visible, as indicated by the color variations in the IPF maps across different strain steps. Some degree of grain shape alteration is also visible. The lattice rotation follows a typical pattern for metallic face-centered cubic materials: grains rotate toward the [001]–[111] line relative to the tensile axis, and, with further strain, toward the [001] and [111] corners of the unit triangle. The changes in the KAM maps reflect the evolution and accumulation of dislocations, particularly within the defect-free channels and at the intersections of these channels with grain boundaries. Overall, the specimen's behavior is consistent with that observed in previously tested irradiated austenitic steels. Further discussion of conventional EBSD results is beyond the scope of this report; more information is available in the literature [4,15] and the references therein.

Figure 10 presents an EBSD map recorded at low magnification, enabling the scanning and analysis of larger areas, covering up to half of the gauge length. This approach allows for locating and tracking the entire neck region.

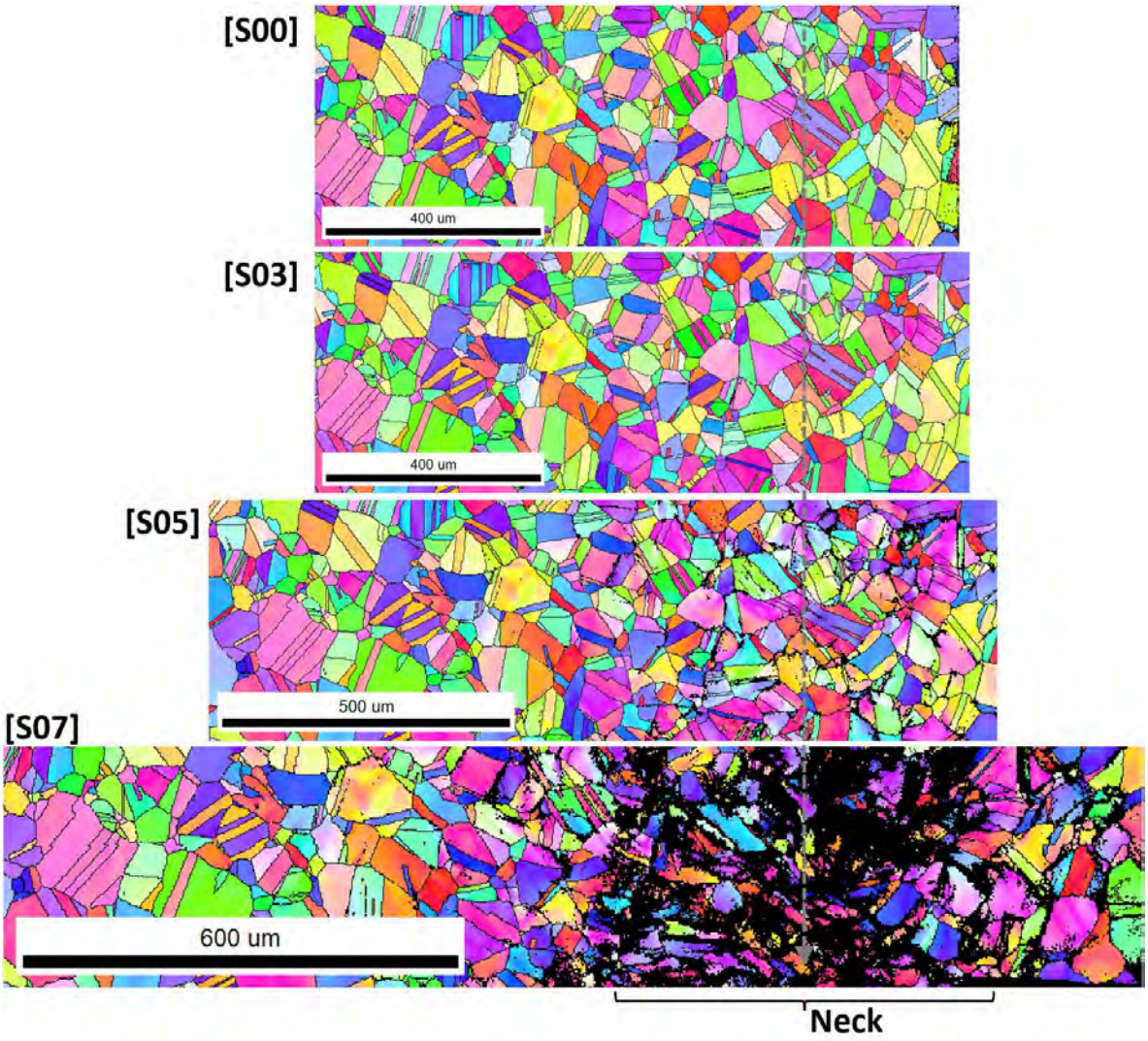

Figure 10. Low-magnification gauge scans showing necking formation. A black bracket indicates the neck location, and a dashed vertical line approximately shows the neck middle.

3.4.2 An Attempt to Visualize Hot Spots and Stationary Deformation Bands

EBSD analysis, combined with in situ mechanical testing, is a powerful tool for detecting strain-induced changes. However, EBSD primarily focuses on crystallographic aspects such as lattice rotation, misorientation gradients, and in-grain dislocation structures, and it cannot directly measure plastic strain. Nevertheless, because of the strong correlation between strain and EBSD-detectable changes in microstructure, EBSD can potentially reveal localized deformation.

Certain EBSD maps, such as the KAM maps in Figure 9, clearly display significant inhomogeneity in strain-induced features. However, local strain values cannot be derived, nor hot spots visualized, as effectively as with DIC maps. Among EBSD's strain metrics, grain average misorientation (GAM) may

be more suitable than KAM because GAM operates on a grain level rather than a kernel or set of neighboring points and may better indicate which grains are more deformed.

Low-magnification SEM/EBSD scanning was performed to assess changes along the gauge. The scan covered an area of 1,200 × 400 μm, providing crystallographic data for nearly half the gauge length. For Specimen 4416-MS-2, the scan also included the neck region.

Figure 11a displays the IPF map for the reference scan; the ROI from Figure 9 is located in the right portion of the scan. Figure 11b shows the GAM map before straining. Although some variations in GAM values are observed, most grains exhibit low GAM values (~0.3°, green color). A cluster of grains, with Grain G_1 as the largest, shows elevated GAM values, likely indicating incomplete recrystallization in this area.

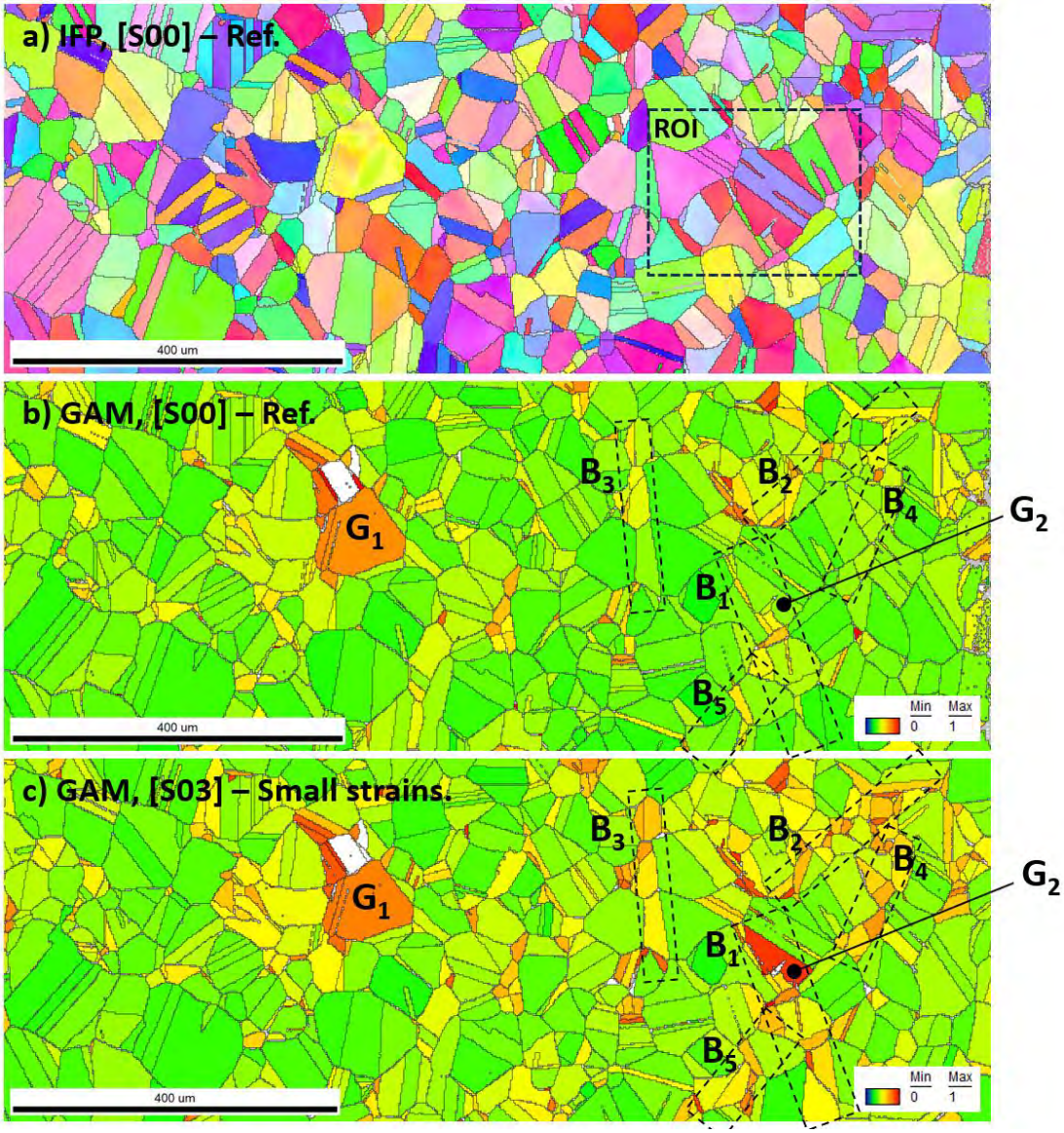

Figure 11. Visualizing hot spots and stationary deformation bands. (a) Reference IPF map for the low-magnification scan (ROI: region of interest shown in Figure 9); (b) grain average misorientation (GAM) map before straining, S00; (c) GAM map at S03 (small plastic strains).

Figure 11c shows the same area after a small plastic strain increment at S03. Changes in some grains (e.g., Grain G_2) are apparent, whereas other grains retained their color, reflecting no or limited strain-induced changes in GAM.

Many grains with pronounced changes group inside the developing neck at the right. Such grains often neighbor each other, forming specific chains or bands. The Bands B_1–B_5 are indicated by dashed rectangles in Figure 11. Mapping the GAM parameter, being helpful with band visualization, provides limited detail on real strain level. Also, localized deformation areas are not necessarily linear structures with uniform strain within the band. More complex strain fields should be expected, especially considering band interaction, leading to spots with elevated strains because of band overlapping. Furthermore, the bands are 3D structures extending into the bulk material, unreachable with EBSD, which is essentially a surface-limited technique. The formation of such structures suggests complex strain transfer between grains.

Many grains exhibiting pronounced changes are grouped within the developing neck on the right side. These grains frequently cluster together, forming distinct chains or bands. The formation of these structures indicates complex strain transfer between grains.

Local strains should be measured and compared with EBSD-derived in-grain changes. However, EBSD maps—particularly those at low magnification—are prone to image distortion, a common issue in SEM. This distortion is sensitive to SEM settings and can fluctuate over time, making strain calculation from EBSD maps difficult. Currently, no tool or method is available to perform such calculations. As a result, strain maps analogous to the DIC maps shown in Figure 4 and Figure 5 are impossible to generate from EBSD data.

3.5 FRACTOGRAPHY ANALYSIS

3.5.1 SEM Results

Following the SEM/EBSD in situ test, Specimen 4416-MS-2 was fractured in air using a conventional tensile frame in LAMDA. The fracture surface was analyzed using a TESCAN MIRA3 SEM instrument. As shown in Figure 12a, b, the fracture region retained a rectangular, nearly square shape. The two halves of the specimen displayed slight geometric differences, indicating significant plastic deformation within the neck region and during the fracture event. Low-magnification images revealed a surface morphology resembling a layered structure, which may reflect the presence of nonmetallic inclusions forming stringers.

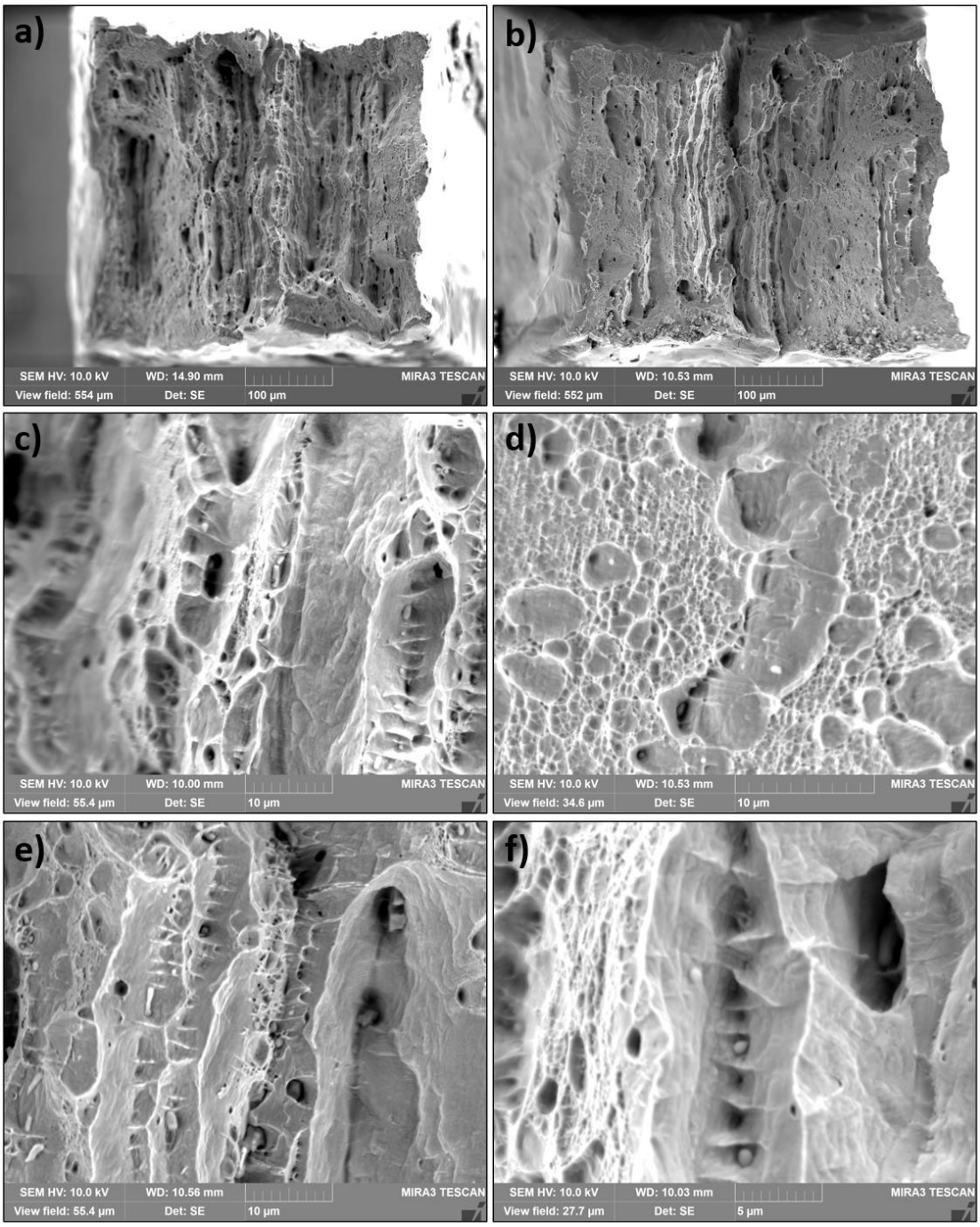

Figure 12. Fractography results for the 4416-MS-2 specimen. : (a, b) Low-magnification images of the fracture areas showing a layered structure in both specimen halves; (c) predominant ductile dimples; (d) ductile shear surface; (e) pronounced ductile and weakly developed cleavage area; (f) small particles inside the dimples.

Images taken at higher magnifications (Figure 12c, d, e) reveal predominantly ductile morphology with minor areas of cleavage fracture. Ductile dimples, formed primarily via tensile fracture (Figure 12c), are accompanied by regions of ductile shear (Figure 12d). In a few small locations, cleavage spots are visible (Figure 12e). High-magnification images frequently show small particles within some dimples (Figure 12f), highlighting a well-known mechanism of dimple formation, in which plastic deformation develops around a pore containing an inclusion.

Figure 13 shows the results of SEM/EDS elemental analysis. Unexpectedly, multiple fine sulfur-rich particles were detected on the fracture surface. Sulfur consistently coexisted with manganese in the EDS maps, indicating that these particles are likely MnS inclusions of metallurgical origin. Several coarse particles exhibited elongated rod-like shapes, measuring approximately 3–4 μm in length, and smaller particles (<1–2 μm) had rounded or irregular shapes. The density and size of the particles suggest a sulfur content exceeding about 0.01%. This result may represent a local fluctuation in the density and size of inclusions confined to this area; additional statistics from other specimens (e.g., from the BS-slice) are required for confirmation.

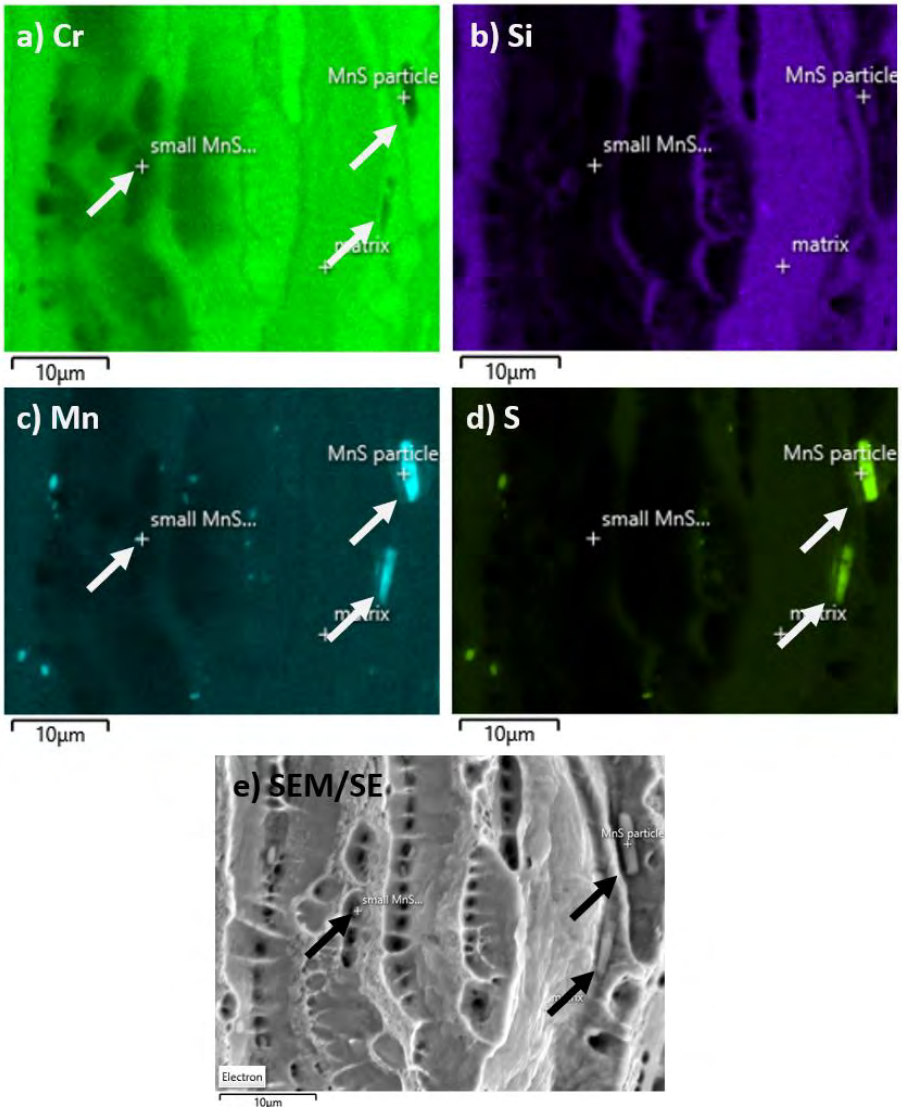

Figure 13. Sulfur-rich particles (likely MnS) at the fracture surface. Chromium and silicon content variations are caused by the developed surface morphology.

3.5.2 TEM/EDS Analysis of the MnS Inclusion

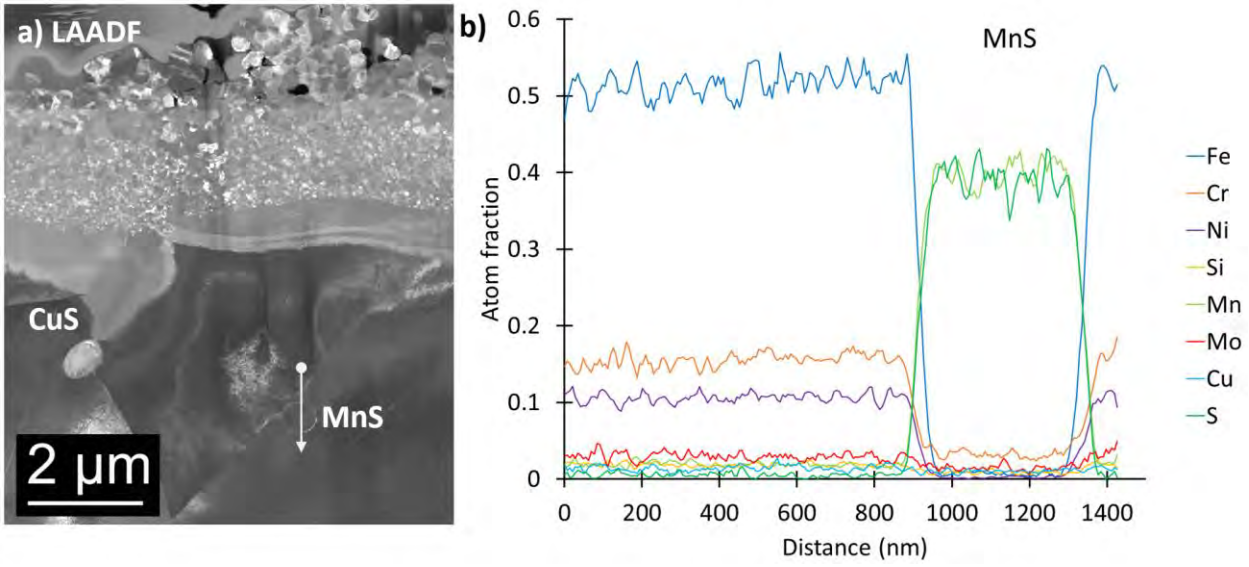

Figure 14. a) TEM image of the microstructure taken near surface in the head-to-shank transition area. Two sulphur-rich inclusions (MnS and CuS) are marked with labels; b) Element profiles (non-normalized atomic fractions) across the MnS-inclusion, see arrow in (a).

One of the sulfur-rich inclusions was observed in a FIB sample taken from the 4416-CS specimen (top portion of the bolt; head-to-shank transition area). TEM offers better spatial resolution compared to SEM, thus providing an opportunity to study element distribution in greater detail.

The inclusion is approximately 0.4 µm in size, as shown in Figure 14a. Element concentration profiles in Figure 14b show nearly equal atomic fractions of Mn and S, with slight enrichment in Cr. Since Mn undergoes transmutation during irradiation in a water-moderated reactor, and considering the high dose, it was expected that at least 1/5 of the initial Mn content would be replaced by Fe as a result of transmutation. However, no significant Fe enrichment was observed. This may suggest diffusion effects, where newly formed iron diffuses out of the inclusion. More work and additional statistics are required to confirm this.

4. MESOSCALE LOCALIZATION MECHANISM AND ITS POSSIBLE EFFECT ON IASCC

The formation of deformed grain chains may facilitate IASCC initiation or generate multiple crack initiation sites. Although dislocation channeling is well documented in the literature as a microscale strain localization mechanism influencing IASCC initiation, mesoscale phenomena (such as groups of interacting grains forming chains or bands) have received limited attention. A literature review revealed an interesting case of intergranular crack formation in thermally sensitized 304 stainless steel subjected to straining in an inert gas atmosphere at 290°C [19]. In addition to analyzing cracking behavior, the authors examined the local strain pattern, showing that cracks formed within localized deformation bands or at their intersections (Figure 15). The authors suggested that radiation-induced plastic deformation localization at the mesoscale (i.e., bands) is a key factor contributing to intergranular cracking in irradiated 304 stainless steel under high-temperature and high-pressure water conditions [19].

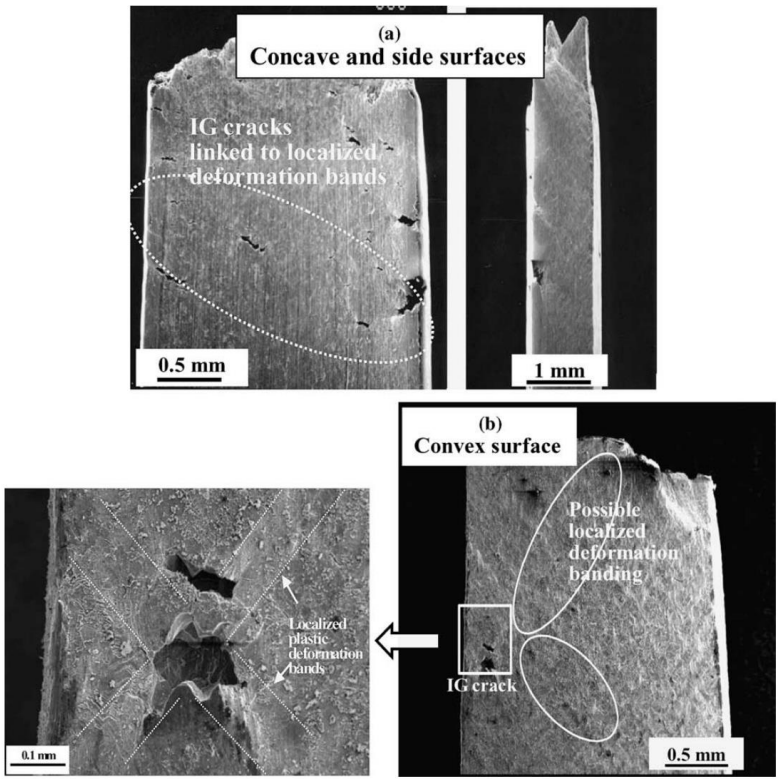

Figure 15. Surface appearances of the thermally sensitized 304 SS specimen, irradiated to 1.2 × 10^{21} n/cm^2 (E > 1 MeV) and after that deformed and fractured in inert gas. (a) Concave and side surfaces and (b) convex surface (after [19]).

5. SUMMARY AND CONCLUSIONS

The study of BFBs irradiated in a commercial PWR provided critical insights into the complex strain localization mechanisms in irradiated austenitic steels that contribute to IASCC. By using advanced testing methods, including DIC, SEM/EBSD analysis, fractography, and TEM/EDS analysis, the research identified the formation of mesoscale deformation bands and hot spots as key features in localized deformation. These bands, often forming chains or clusters of grains, developed early during plastic deformation and persisted throughout much of the strain evolution. Although dislocation channeling at the microscale has been well-studied in relation to IASCC, the mesoscale deformation behavior, in which multiple grains interact to form hot spots and short deformation bands, has received less attention. The findings from this study suggest that these mesoscale structures may play a significant role in facilitating crack initiation in irradiated austenitic stainless steels.

The fracture mechanism for the studied highly irradiated austenitic steel may be characterized as dominating ductile dimples coexisting with small brittle cleavage spots. Fractography analysis revealed the presence of sulfur-rich MnS inclusions at the fracture surface. TEM analysis performed on FIB lift out confirmed the presence of MnS inclusions. These inclusions, combined with the complex strain localization patterns, highlight potential factors that could exacerbate crack initiation.

Overall, the research emphasizes the need for a deeper understanding of mesoscale deformation mechanisms and their effect on the integrity of PWR components. By shedding light on the role of localized strain behavior in IASCC, this study supports ongoing efforts to improve the long-term performance and reliability of nuclear reactor materials, especially as the industry seeks to extend the operational lifetimes of existing reactors.

REFERENCES

[1] K.J. Leonard, M.A. Sokolov, M.N. Gussev, Post-Service Examination of PWR Baffle Bolts, Part I. Examination and Test Plan, Oak Ridge National Laboratory Report, ORNL/LTR-2015/193, 2015.

[2] X.F. Chen, M.A. Sokolov, Fracture Toughness and Fatigue Crack Growth Rate Testing of Baffle-Former Bolts Harvested from a Westinghouse Two-Loop Downflow Type PWR, Oak Ridge National Lab.(ORNL), Oak Ridge, TN (United States), 2021.

[3] T. Lach, X. Chen, T.M. Rosseel, Microstructural Characterization of the Second High Fluence Baffle-Former Bolt Retrieved from a Westinghouse Two-loop Downflow Type PWR, Oak Ridge National Lab.(ORNL), Oak Ridge, TN (United States), 2022.

[4] X.F. Chen, T. Chen, C.M. Parish, T. Graening, M.A. Sokolov, K.J. Leonard, Post-Irradiation Examination of High Fluence Baffle-Former Bolts Retrieved from a Westinghouse Two-Loop Downflow Type PWR, Oak Ridge National Lab.(ORNL), Oak Ridge, TN (United States), 2019.

[5] M. Gussev, Dixon, Travis, Chen, Xiang, Analysis of Deformation and Fracture Mechanisms in the Harvested Low-Dose Baffle Former Bolt via Advanced Mechanical Tests, Oak Ridge National Lab.(ORNL), Oak Ridge, TN (United States), 2023.

[6] T.G. Lach, M.N. Gussev, X. Chen, Complexity of segregation behavior at localized deformation sites formed while in service in a 316 stainless steel baffle-former bolt, subbmitted to Scripta Materialia (n.d.).

[7] O.K. Chopra, A.S. Rao, Degradation of LWR Core Internal Materials due to Neutron Irradiation, 2010.

[8] M.N. Gussev, E. Cakmak, K.G. Field, Impact of neutron irradiation on mechanical performance of FeCrAl alloy laser-beam weldments, Journal of Nuclear Materials 504 (2018) 221–233. https://doi.org/10.1016/j.jnucmat.2018.03.036.

[9] M. Sutton, J. Orteu, H. Schreier, Digital image correlation (DIC), Image Correlation for Shape, Motion and Deformation Measurements: Basic Concepts, Theory and Applications (2009).
[10] B. Pan, Digital image correlation for surface deformation measurement: historical developments, recent advances and future goals, Measurement Science and Technology 29 (2018) 082001.
[11] H. Bruck, S. McNeill, M.A. Sutton, W. Peters, Digital image correlation using Newton-Raphson method of partial differential correction, Experimental Mechanics 29 (1989) 261–267.
[12] B. Pan, Recent progress in digital image correlation, Experimental Mechanics 51 (2011) 1223–1235.
[13] W. Tong, Formulation of Lucas–Kanade digital image correlation algorithms for non-contact deformation measurements: a review, Strain 49 (2013) 313–334.
[14] M.N. Gussev, D.A. McClintock, T.S. Byun, T.G. Lach, Recent progress in analysis of strain-induced phenomena in irradiated metallic materials and advanced alloys using SEM-EBSD in-situ tensile testing, Current Opinion in Solid State and Materials Science 28 (2024) 101132.
[15] M.N. Gussev, K.J. Leonard, In situ SEM-EBSD analysis of plastic deformation mechanisms in neutron-irradiated austenitic steel, Journal of Nuclear Materials 517 (2019) 45–56.
[16] M.N. Gussev, K.G. Field, J.T. Busby, Deformation localization and dislocation channel dynamics in neutron-irradiated austenitic stainless steels, Journal of Nuclear Materials 460 (2015) 139–152.
[17] R. Ambriz, C. Froustey, G. Mesmacque, Determination of the tensile behavior at middle strain rate of AA6061-T6 aluminum alloy welds, International Journal of Impact Engineering 60 (2013) 107–119.
[18] T. Poletika, A. Pshenichnikov, Non-linear macrolocalization of strain in hexagonal close-packed zirconium alloys, Technical Physics 54 (2009) 380–384.
[19] T. Onchi, K. Dohi, N. Soneda, M. Navas, M.L. Castaño, Mechanism of irradiation assisted stress corrosion crack initiation in thermally sensitized 304 stainless steel, Journal of Nuclear Materials 340 (2005) 219–236.